

NEW MEASUREMENTS OF THE MOTION OF THE ZODIACAL DUST

R. J. REYNOLDS AND G. J. MADSEN

Department of Astronomy, 475 North Charter Street, University of Wisconsin at Madison, Madison, WI 53706;
reynolds@astro.wisc.edu, madsen@astro.wisc.edu

AND

S. H. MOSELEY

Code 685, Infrared Astrophysics Branch, Goddard Space Flight Center, Greenbelt, MD 20771; moseley@stars.gsfc.nasa.gov

Received 2003 December 17; accepted 2004 May 20

ABSTRACT

Using the Wisconsin H α Mapper (WHAM), we have measured at high spectral resolution and high signal-to-noise ratio the profile of the scattered solar Mg I λ 5184 Fraunhofer line in the zodiacal light. The observations were carried out toward 49 directions that sampled the ecliptic equator from solar elongations of 48° (evening sky) to 334° (morning sky) plus observations near +47° and +90° ecliptic latitude. The spectra show a clear prograde kinematic signature that is inconsistent with dust confined to the ecliptic plane and in circular orbits influenced only by the Sun's gravity. In particular, the broadened widths of the profiles, together with large amplitude variations in the centroid velocity with elongation angle, indicate that a significant population of dust is on eccentric orbits. In addition, the wide, flat-bottomed line profile toward the ecliptic pole indicates a broad distribution of orbital inclinations extending up to about 30°–40° with respect to the ecliptic plane. The absence of pronounced asymmetries in the shape of the profiles limits the retrograde population to less than 10% of the prograde population, and also places constraints on the scattering phase function of the particles. These results do not show the radial outflow or evening-morning velocity amplitude asymmetry reported in some earlier investigations. The reduction of the spectra included the discovery and removal of extremely faint, unidentified terrestrial emission lines that contaminate and distort the underlying Mg I profile. This atmospheric emission is too weak to have been seen in earlier, lower signal-to-noise ratio observations, but it probably affected the line centroid measurements of previous investigations.

Subject headings: interplanetary medium — line: profiles — scattering — solar system: general

1. INTRODUCTION

The motion of interplanetary dust particles orbiting the Sun contains clues about their origin and the nongravitational forces affecting their lifetimes in the solar system, with potential relevance to dust disks surrounding other stars (e.g., Mann et al. 1996; Dermott et al. 1994). A more accurate understanding of this “zodiacal cloud” can also affect studies of faint Galactic and extragalactic backgrounds (e.g., Haffner et al. 2003; Bernstein et al. 2002; Kelsall et al. 1998). In theory, Doppler shifts of scattered solar Fraunhofer lines in the zodiacal light provide an opportunity to explore and monitor the large-scale kinematics of interplanetary dust in the inner solar system through ground-based spectroscopic techniques (e.g., Ingham 1963; James 1969, 1996; Hirschi & Beard 1987; Clarke et al. 1996), which would be an important complement to studies of the zodiacal brightness distribution and the in situ detection of interplanetary particles by spacecraft (Mann 1998; Grün et al. 1997). In practice, the faint, spatially extended nature of the zodiacal light, combined with the requirements of both high signal-to-noise ratio and high spectral resolution to measure the predicted subtle changes in the position and shape of the line, have made these observations difficult to carry out.

Early attempts that targeted the H β λ 4861 line (e.g., Clarke et al. 1967; Daehler et al. 1968; Reay & Ring 1969) encountered the additional problem that the absorption line was severely contaminated by emission originating from atomic hydrogen in the Earth's atmosphere and the Galaxy's interstellar medium (Reynolds et al. 1973). This led investigators to

concentrate their observations on other lines (James & Smeeth 1970; Hicks et al. 1974; Fried 1978; East & Reay 1984), especially the Mg I line at 5183.62 Å, which has a large equivalent width and seemed to have no contaminating atmospheric emission. However, except for the conclusion that the motion was primarily prograde, the resulting information about the orbital properties of the dust was uncertain and contradictory (see a summary of the situation by Clarke et al. 1996).

One of the principal difficulties with these earlier observations was the insufficient throughput of the spectrometers. This resulted in low signal-to-noise ratio data and thus prevented precise measurements of line centroids and shapes, particularly at large solar elongations and at high ecliptic latitudes, where the zodiacal emission is faintest but where observations are crucial for comparisons with predictions of kinematic models. Below, we present new, high signal-to-noise ratio observations of the Mg I λ 5184 line in the zodiacal light using the Wisconsin H α Mapper (WHAM) Fabry-Pérot facility at the National Optical Astronomy Observatory on Kitt Peak in Arizona. WHAM's unprecedented combination of high throughput and high spectral resolution reveals clearly resolved Mg I line profiles that are shifted and broadened by the motion of the zodiacal dust.

2. THE WISCONSIN H α MAPPER OBSERVATIONS

WHAM consists of a 15 cm aperture, dual-etalon Fabry-Pérot spectrometer coupled to a high-efficiency CCD camera and fed by a dedicated 0.6 m telescope. The dual-etalon design, when compared to traditional single-etalon Fabry-Pérot

systems, provides superior ghost and order rejection, extends the free spectral range, and suppresses the Lorentzian-like wings of the spectral response function. The CCD is used as a multichannel detector to record a 12 km s^{-1} (0.2 \AA at 5184 \AA) resolution spectrum over a 200 km s^{-1} (3.5 \AA) spectral window that can be centered on any wavelength between 4800 and 7300 \AA . The 15 cm diameter etalons provide maximum throughput, which when combined with the 0.6 m aperture telescope results in a 1.0 diameter beam on the sky.

Although built and operated primarily for studies of faint diffuse emission lines, particularly $\text{H}\alpha$ from the Galaxy's interstellar medium, WHAM is ideally suited for high spectral resolution observations of any faint spatially extended source in the night sky, including comets (Morgenthaler et al. 2001), the Earth's atmosphere (Nossal et al. 2001), and the zodiacal light. The facility is completely remotely operated, and all the observations presented here were obtained with WHAM controlled from Madison, Wisconsin. Additional information about WHAM can be found in Haffner et al. (2003) and Tufté (1997).

Spectra centered on $\text{Mg I } \lambda 5184$ were obtained on the two moonless nights of 2002 November 4 and 5. The spectra sample 49 directions near the ecliptic equator between elongations $\epsilon = 47.5^\circ$ (evening sky) and $\epsilon = 333.9^\circ$ (26.1° west of the Sun in the morning sky). Two directions at high ecliptic latitude were also observed, $\epsilon \approx 272^\circ$, $\beta \approx +47^\circ$ and the north ecliptic pole (NEP). In addition, observations of the relatively bright twilight sky were obtained to provide a calibration spectrum close to representing the unperturbed solar line profile. The directions of the zodiacal observations and the integration time for each spectrum are listed in the first three columns of Table 1. A 30° gap in the data near elongation 225° is due to interference by stars near the plane of the Milky Way, which produced anomalies in the spectra. The Galactic plane intersected the ecliptic plane at $\epsilon = 50^\circ$ and $\epsilon = 230^\circ$ at Galactic longitudes 6° and 186° , respectively.

A twilight spectrum is shown in Figure 1. The absorption feature is dominated by the Mg I line at 5183.62 \AA , with weak contributions from Fe I at 5184.27 \AA and Cr I at 5184.59 \AA . A potential problem in using twilight spectra to represent the unperturbed source spectrum is the contamination of the daylight and twilight Fraunhofer lines by a pseudo-continuum emission from inelastic scattering (i.e., rotational Raman scattering) of sunlight by atmospheric nitrogen and oxygen molecules. Both observations and theory suggest that this so-called Ring effect tends to fill in the Fraunhofer lines at about the 10% level with minimal change to the width of the line (e.g., Grainger & Ring 1962; Pallamraju et al. 2000; Sioris & Evans 1999; Kattawar et al. 1981). To investigate this we compare our twilight spectrum in Figure 1 with a high-resolution unscattered solar spectrum convolved with WHAM's 12 km s^{-1} wide spectral response profile. After scaling to match the "continua" and the profile minima within the observed spectral interval, we found the profiles to be nearly coincident (see Fig. 1). Thus, both the twilight profile and the convolved direct solar profile appear to be good representations of the unperturbed solar spectrum and useful for comparison with the Doppler-perturbed zodiacal profiles. The Ring effect, a phenomenon affecting the spectrum of sunlight that has been scattered by atmospheric molecules, is not relevant to the zodiacal light, which is scattered by interplanetary dust particles. Zero on the abscissa in Figure 1 and in all following spectra is defined by the centroid of the core of the Mg I component in the twilight spectra, with a small ($\sim 0.2 \text{ km s}^{-1}$) correction for the observed

Doppler shifts associated with the Earth's rotation. The uncertainty in this calibration is less than $\pm 0.02 \text{ \AA}$ ($\pm 1 \text{ km s}^{-1}$).

3. THE ZODIACAL SPECTRA

3.1. Contamination by Weak Atmospheric Emission Lines

The average spectrum east of the Sun near $\epsilon \approx 100^\circ$ and the average spectrum at the corresponding elongation west of the Sun near $\epsilon \approx 260^\circ$ are shown superposed in Figure 2a. The prograde kinematic signature of the zodiacal dust is clearly seen, with the profile in the evening spectrum (*triangles*) redshifted and the profile in the morning spectrum (*circles*) blueshifted with respect to the centroid of the unperturbed solar Mg I line. However, in addition to being shifted (and broadened) these spectra exhibit a number of extremely weak, relatively narrow emission lines. The fact that these emission features are present at the same wavelengths in both of the spectra in Figure 2a implies that they are not associated with the Doppler-shifted light from the zodiacal dust and instead originate from the Earth's atmosphere. This emission could be associated with O II bands, which populate this region of the spectrum (T. G. Slanger 2004, private communication; Huestis et al. 2001). Previous studies of interstellar emission with WHAM have shown that such weak (intensities $\lesssim 0.1 R^1$), unidentified atmospheric emission lines are present throughout the visible spectrum (e.g., Hausen et al. 2002; G. J. Madsen et al. 2004, in preparation). They distort the shapes of observed zodiacal and interstellar line profiles, modify their measured intensities and equivalent widths, and in observations with insufficient spectral resolution produce a pseudo-continuum on the order of $10^{-8} \text{ ergs cm}^{-2} \text{ s}^{-1} \text{ sr}^{-1} \text{ \AA}^{-1}$. Therefore, before proceeding with the analysis of the zodiacal line profiles it was necessary to remove this contaminating terrestrial emission from each spectrum.

To characterize more accurately the spectrum of this foreground emission, all spectra in directions with the faintest zodiacal emission (i.e., $88^\circ < \epsilon < 272^\circ$) were averaged together, producing the very high signal-to-noise ratio composite spectrum in Figure 2b, where all the zodiacal absorption features, including the Fe and Cr lines, are highly Doppler broadened into a single, smooth profile. From this spectrum it was possible to identify the narrow terrestrial emission features against the underlying, Doppler-smearing zodiacal spectrum by fitting a smooth, single-Gaussian profile to the spectrum in Figure 2b in such a way that the residuals were near zero or positive at all velocities. The residuals, indicated by the solid line in Figure 2c, thus represent the spectrum of the foreground terrestrial emission. The sharpness of the features in Figure 2c provides additional confirmation that they are not associated with the highly broadened zodiacal profile. Also plotted in Figure 2c are the maximum and minimum allowed terrestrial emission spectra that are consistent with the spectrum in Figure 2b.

Although too weak to have been identified in earlier, lower signal-to-noise ratio observations, this terrestrial emission, if not removed, would clearly distort the apparent centroid and shape of the underlying zodiacal absorption feature (see Fig. 4a). Therefore, to obtain uncontaminated zodiacal profiles we subtracted the best-fitted terrestrial emission spectrum (solid line in Fig. 2c) from each of the spectra listed in Table 1. This process treated each spectrum the same and did not take into account possible temporal variations in the intensity of

¹ $R = 10^6/4\pi \text{ photons s}^{-1} \text{ cm}^{-2} \text{ sr}^{-1}$.

TABLE 1
SUMMARY OF OBSERVATIONS AND RESULTS

ϵ (deg)	β (deg)	Time (s)	V (km s ⁻¹)	ΔV_{\min} (km s ⁻¹)	ΔV_{\max} (km s ⁻¹)	W (km s ⁻¹)	ΔW_{\min} (km s ⁻¹)	ΔW_{\max} (km s ⁻¹)	A (R)	ΔA_{\min} (R)	ΔA_{\max} (R)
47.5.....	0.0	240	-3.4	-0.5	+0.5	80.3	-1.4	+1.3	-1.67	-0.04	+0.05
57.5.....	0.0	120	+2.1	-0.6	+0.7	76.1	-0.3	+0.5	-1.27	-0.01	+0.03
57.9.....	0.0	600	+2.8	-0.6	+0.6	74.1	-0.2	+0.2	-1.31	-0.01	+0.01
67.5.....	0.0	240	+5.7	-0.6	+0.5	78.1	-1.3	+1.3	-1.24	-0.04	+0.04
67.9.....	0.0	600	+6.7	-0.8	+0.8	75.6	+0.3	-0.4	-0.98	0.00	0.00
72.5.....	0.0	120	+10.9	-0.8	+0.8	78.2	+1.3	-1.4	-0.95	+0.01	-0.01
77.5.....	0.0	120	+10.3	-0.8	+0.8	80.1	-1.6	+1.5	-0.78	-0.04	+0.04
77.9.....	0.0	1800	+9.1	-1.0	+1.0	74.4	+0.7	-0.9	-0.77	0.00	0.00
82.5.....	0.0	120	+9.5	-1.1	+1.1	82.1	+2.0	-2.1	-0.79	+0.01	-0.01
87.5.....	0.0	120	+12.2	-1.2	+1.1	79.1	+1.9	-2.1	-0.70	+0.01	-0.01
87.9.....	0.0	600	+12.1	-0.8	+0.7	74.8	-1.7	+1.6	-0.68	-0.04	+0.04
92.5.....	0.0	120	+14.1	-1.1	+1.1	81.8	+2.5	-2.6	-0.73	+0.01	-0.01
97.8.....	0.0	600	+11.6	-0.7	+1.2	73.1	-1.6	+2.4	-0.57	-0.04	+0.05
107.8.....	0.0	600	+12.8	-1.4	+1.3	69.7	+1.9	-2.2	-0.49	0.00	0.00
127.9.....	0.1	600	+11.7	-1.5	+1.4	74.5	+2.3	-2.5	-0.50	0.00	-0.01
137.5.....	0.0	120	+6.5	-1.6	+1.6	87.2	+2.6	-3.0	-0.67	+0.02	-0.02
137.8.....	0.0	600	+10.9	-1.1	+1.0	72.9	-2.4	+2.2	-0.49	-0.04	+0.04
147.8.....	0.0	600	+10.5	-1.3	+1.3	69.8	+1.3	-1.6	-0.52	0.00	0.00
157.8.....	0.0	600	+6.9	-1.2	+1.1	72.8	-3.1	+2.8	-0.52	-0.04	+0.04
167.8.....	0.0	600	+2.8	-1.2	+1.2	70.1	-3.4	+3.0	-0.47	-0.04	+0.04
169.2.....	0.0	120	+1.4	-1.3	+0.8	78.7	-3.7	+2.8	-0.57	-0.05	+0.04
174.2.....	0.0	120	-0.3	-1.1	+1.0	83.9	-3.0	+2.8	-0.66	-0.04	+0.05
177.8.....	0.0	600	+0.9	-1.0	+1.3	75.4	-3.0	+3.3	-0.56	-0.04	+0.05
179.3.....	0.0	120	-1.3	-1.0	+1.0	65.6	-3.6	+3.4	-0.53	-0.04	+0.04
184.2.....	0.0	120	-1.6	-1.2	+1.0	71.2	-3.6	+3.1	-0.52	-0.04	+0.04
187.8.....	0.0	600	-0.8	-1.2	+1.2	77.2	-3.9	+3.6	-0.54	-0.04	+0.04
189.2.....	0.0	120	-4.1	-1.1	+1.1	84.5	-3.4	+3.1	-0.62	-0.04	+0.04
197.8.....	0.0	600	-0.4	-1.2	+1.1	73.4	-3.7	+3.5	-0.51	-0.04	+0.04
207.8.....	0.0	600	-3.9	-1.3	+1.3	75.2	-4.3	+3.9	-0.50	-0.04	+0.04
239.0.....	2.0	300	-8.2	-1.2	+1.2	75.4	-4.2	+4.0	-0.53	-0.04	+0.04
244.0.....	2.0	300	-11.0	-1.2	+1.3	80.9	-1.6	+1.5	-0.59	-0.01	+0.01
249.0.....	2.0	300	-10.7	-1.1	+1.2	81.4	-4.7	+4.5	-0.57	-0.04	+0.05
252.1.....	0.0	600	-10.9	-1.1	+1.1	80.4	-4.6	+4.3	-0.59	-0.04	+0.05
254.0.....	2.0	300	-10.7	-0.9	+1.1	78.4	-5.0	+4.5	-0.57	-0.04	+0.04
262.1.....	0.0	1800	-10.2	-0.9	+1.2	78.8	-1.2	-3.2	-0.74	-0.01	-0.06
264.0.....	2.0	300	-12.8	-0.6	+1.6	77.3	-3.9	+5.2	-0.57	-0.04	+0.05
282.0.....	0.0	600	-10.7	-0.8	+0.8	77.7	-3.2	+3.2	-0.77	-0.04	+0.04
283.9.....	2.0	300	-8.2	-0.9	+0.9	73.2	-3.5	+3.3	-0.67	-0.04	+0.04
288.9.....	2.0	300	-7.7	-0.8	+0.8	77.2	-3.0	+2.9	-0.82	-0.04	+0.04
293.9.....	2.0	300	-7.0	-0.8	+0.8	76.8	-2.8	+2.7	-0.84	-0.04	+0.04
298.9.....	2.0	300	-5.4	-0.7	+0.7	74.0	-2.6	+2.4	-0.90	-0.04	+0.04
303.9.....	2.0	300	-2.8	-0.6	+0.7	77.1	-0.5	+0.4	-1.15	-0.01	+0.01
308.9.....	2.0	300	-2.0	-0.6	+0.6	77.2	-0.4	+0.3	-1.32	-0.01	+0.01
312.0.....	0.0	600	-1.0	-0.4	+0.4	74.9	-0.3	+0.3	-1.94	-0.01	+0.01
313.9.....	2.0	300	+0.4	-0.5	+0.5	74.8	-0.3	+0.2	-1.58	-0.01	+0.01
318.9.....	2.0	300	+2.2	-0.4	+0.4	73.6	-0.2	+0.1	-1.84	-0.01	+0.01
323.8.....	2.0	300	+5.1	-0.3	+0.3	77.0	+0.1	-0.1	-2.45	-0.00	0.00
328.9.....	2.0	300	+7.6	-0.2	+0.2	75.2	+0.1	-0.1	-3.07	-0.00	+0.01
333.9.....	2.0	300	+8.5	-0.2	+0.2	76.1	+0.1	-0.1	-5.06	0.00	0.00
NEP.....	90.0	2580	-2.2	-2.5	+2.5	83.2	+0.4	-0.4	-0.36	0.00	+0.01
272.....	47	1800	-3.2	-2.1	+2.1	77.3	+1.4	-1.4	-0.39	+0.01	-0.01
Twilight.....	0.0	58.2

NOTE.— ΔX_{\min} (ΔX_{\max}) is the change in the corresponding value if the minimal (maximal) correction is used for the atmospheric lines, i.e., $\Delta X_{\min} = X_{\min} - X$ (see § 3).

this emission or variations in the relative strengths of the individual emission components. However, because the emission is extremely weak there was no way to identify and remove it from each spectrum independently. When the observations were separated by halves of the night, by day, and by high and low ecliptic latitude, the best-fit spectrum in Figure 2c provided good removal of the emission features

within the uncertainties, suggesting that this spectrum closely approximates the terrestrial contamination in each individual spectrum.

3.2. Pure Zodiacal Spectra

Figure 3 shows a sample spectrum after removal of the contaminating atmospheric emission as described above. The

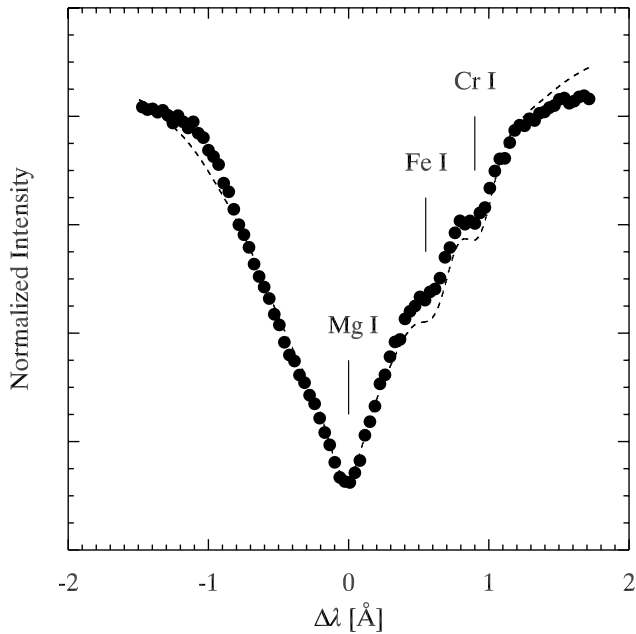


FIG. 1.—Unperturbed solar spectrum from the bright twilight sky (circles), showing the Mg I profile plus the two weaker, narrower lines from Fe I and Cr I. For comparison, the dashed curve shows the direct, high-resolution solar spectrum from Delbouille et al. (1973) convolved with WHAM's spectral response function (see § 2).

abscissa is in units of radial velocity, where zero corresponds to the centroid of the unperturbed Mg I $\lambda 5184$ component in the solar spectrum (Fig. 1). To obtain the centroid velocity (V), FWHM (W), and area (A) of the zodiacal Mg I absorption component, a least-squares three-Gaussian fit, representing the Mg I and the two weak Fe I and Cr I features, was made to the spectrum. During the fit the relative centroid positions and the relative areas of the three components were held fixed at the values found in the twilight spectrum, and the widths of the two minor Fe I and Cr I features were held fixed at 55 km s^{-1} , the approximate mean broadening of the zodiacal spectra. The fitting procedure also took into account the 12 km s^{-1} wide instrumental response function of the WHAM spectrometer and a small correction for Doppler shifts due to the Earth's rotation. The resulting best fit (solid curve) and residuals are included in Figure 3. Values for the best-fit parameters of the Mg I component for this and all the other spectra are listed in Table 1.

The resulting radial velocities, widths, and areas of the Mg I component along the ecliptic equator are plotted in Figures 4a, 4b, and 4c, respectively. The uncertainties associated with these results are the combined uncertainty associated with random errors due to Poisson noise, the placement of the continuum, plus the systematic error associated with the subtraction of the atmospheric emission. In this last case the error was estimated by fitting each spectrum two more times, after subtracting the “minimal” and “maximal” versions of the atmospheric emission spectrum (Fig. 2c). We found that the uncertainty in the radial velocity is dominated by the systematic error associated with the removal of the atmospheric emission and that errors in the widths and areas are dominated by the uncertainty in the placement of the continuum. The uncertainties listed in Table 1 and plotted in Figures 4a and 4b indicate only the systematic error due to the removal of the atmospheric emission. In most observations, the subtraction of the minimal (maximal) terrestrial spectrum instead of

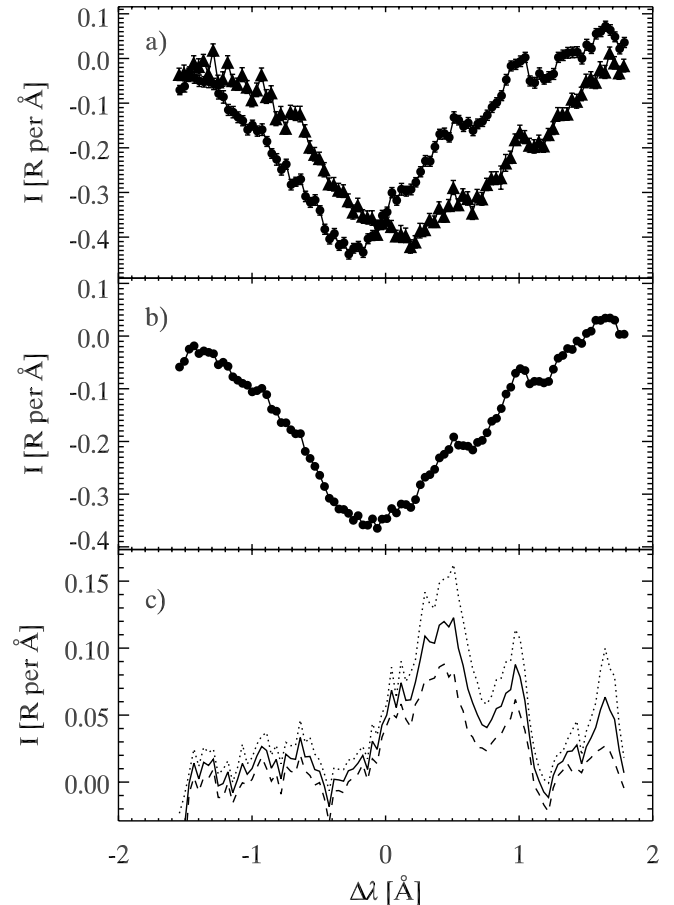


FIG. 2.—(a) Average spectrum between $\epsilon \approx 88^\circ$ and 108° (circles) and the average spectrum between $\epsilon \approx 252^\circ$ and 264° (triangles), showing weak, narrow, unshifted terrestrial emission lines superposed on the scattered solar profile, broadened and shifted by the motion of the zodiacal dust. (b) Average of all spectra between elongations 88° and 264° , which shows more clearly the contaminating terrestrial emission lines superposed on the kinematically smeared, high signal-to-noise ratio zodiacal spectrum. (c) Best-fit (solid line) atmospheric emission spectrum extracted from the spectrum in Fig. 2b (see text). The dotted line represents the maximal atmospheric contamination and the dashed line the minimal atmospheric contamination consistent with the spectrum in Fig. 2b. $1 \text{ R } \text{\AA}^{-1}$ corresponds to $3 \times 10^{-7} \text{ ergs cm}^{-2} \text{ s}^{-1} \text{ sr}^{-1} \text{ \AA}^{-1}$ at 5184 \AA .

the “best” terrestrial spectrum results in systematically less (more) positive centroid velocities, narrower (wider) line widths, and slightly larger (smaller) areas. Also plotted are the resulting velocities (open squares in Fig. 4a) when *no* correction was made for the atmospheric emission, to illustrate the significant effect this emission can have on the derived results if it is not removed from the spectra. The effect on W and A is less dramatic, due in part to the fact that, while some of the emission lines fill in the zodiacal absorption profile slightly, other lines raise the “continuum.” The scatter in the values for the line widths and areas, which is significantly larger than the plotted (systematic) error, reflects primarily the uncertainties in W and A associated with continuum placement.

Figure 4a reveals a well-characterized velocity versus elongation kinematic signature for the line centroids indicative of prograde orbits, and Figure 4b shows significant broadening of the line profiles with respect to the unperturbed solar spectrum at all elongations, including 180° . The radial velocities pass through zero at $\epsilon \approx 54^\circ$, near 180° , and at $\epsilon \approx 315^\circ$, indicating a small (10°) evening-morning asymmetry in the elongation at which the radial velocity passes through zero.

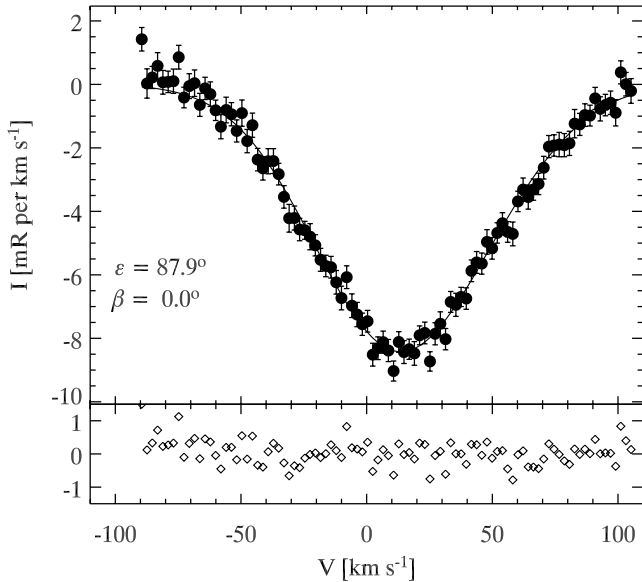


FIG. 3.—Sample spectrum of the zodiacal light toward $\epsilon \approx 88^\circ$ with the terrestrial emission removed. The integration time was 600 s. The best three-Gaussian (Mg I, Fe I, and Cr I) fit (solid line) and the resulting residuals are also indicated. The error bars represent the $\pm 1 \sigma$ Poisson noise.

These data show no evidence for a general outflow (i.e., a mean positive velocity shift at 180°) or an evening-morning asymmetry in the velocity amplitudes as reported in some earlier studies (East & Reay 1984; Hicks et al. 1974). Within the uncertainty associated with the removal of the atmospheric emission (see above), the radial velocity at 180° is consistent with zero and the maximum amplitudes of the radial velocities are antisymmetric, reaching approximately $+13 \text{ km s}^{-1}$ at $\epsilon \approx 100^\circ$ and approximately -12 km s^{-1} at $\epsilon \approx 260^\circ$. The area of the Mg I absorption profile is a tracer of the zodiacal continuum intensity, and Figure 4c shows evidence for the gegenschein and the steep rise in zodiacal intensity for directions within $\sim 70^\circ$ of the Sun. The absolute intensity calibration of these observations is accurate to only $\sim 20\%$, and zero intensity relative to the continuum is uncertain because of an added flat continuum from parasitic (out of band) light. Because the intensity distribution of the zodiacal light has been well studied by others, the remainder of this paper focuses on some of the implications of the new kinematic information revealed by the radial velocities and line widths of the Mg I profile presented in Figures 4a and 4b.

4. DISCUSSION

4.1. Orbital Eccentricities

The orbital properties of the zodiacal dust, including the eccentricity, inclination, and the effect of radiation pressure, can be explored by comparing these results with line profiles and Doppler shifts calculated from models of the distribution, kinematics, and scattering properties of the dust (e.g., James 1969; Reay 1969; Bandermann & Wolstencroft 1969; Rodriguez & Magro 1978; Hirschi 1985; Hirschi & Beard 1987; Mukai & Mann 1993; Clarke et al. 1996). In Figure 5, the observed velocity centroids V and line widths W are compared with models by Hirschi & Beard (1987) and Hirschi (1985), who have made the most detailed predictions of these two parameters. They considered a variety of models with isotropically scattering particles in prograde orbits confined to the ecliptic plane. We consider four of their models here: model *a*, particles on circular

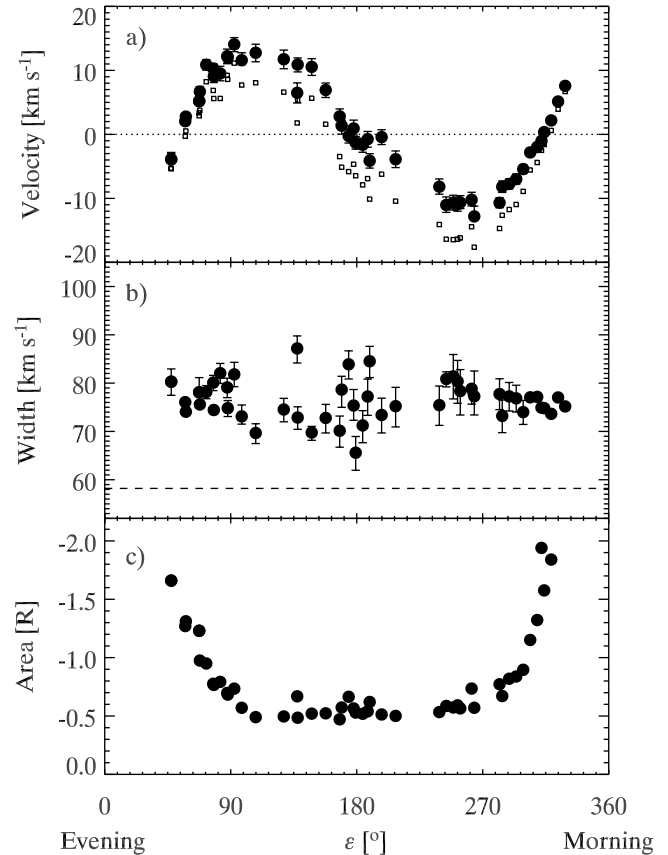


FIG. 4.—Best-fit centroid radial velocity (V), FWHM (W), and area (A) for the Mg I line are plotted for each of the zodiacal spectra near the ecliptic equator. The error bars represent the systematic uncertainty listed in Table 1 associated with the removal of the contaminating atmospheric emission (see § 3). The open squares in *a* show the resulting velocities if the atmospheric emission is not removed. The dashed line in *b* represents the width of the Mg I component in the unperturbed solar spectrum.

orbits and influenced only by solar gravity; model *b*, particles on elliptical orbits having a uniform distribution of eccentricities between 0 and 1; model *c*, particles on elliptical orbits with a distribution of eccentricities weighted toward low eccentricities; and model *d*, particles on circular orbits but influenced by radiation pressure, that is, experiencing a lower effective gravity. These models are represented by the solid, dotted, dot-dashed, and dashed curves, respectively, in Figure 5.

The data clearly rule out pure circular orbits (model *a*; solid line). The predicted amplitude of the radial velocity variations is too small, the elongations at which the predicted radial velocity curve passes through zero are too far from the Sun, and the widths of the predicted profiles are too narrow to fit the observations. Particles in circular orbits, but moving at sub-Keplerian speeds because of radiation pressure (model *d*; dashed line), would exhibit a larger radial velocity amplitude and intercept zero velocity closer to the Sun (Fig. 5a), depending on the magnitude of the effect. However, the predicted line widths from such circularly orbiting dust would still remain far too narrow to fit the observations (Fig. 5b).

These results agree best with models in which the zodiacal dust is moving on elliptical orbits. This conclusion is supported most convincingly by the observed broadening of the line profiles. As pointed out by Hirschi & Beard (1987), it is the line widths, especially near elongation 180° , that clearly distinguish spectra of elliptically orbiting dust from spectra of dust in circular orbits, including dust in circular orbits

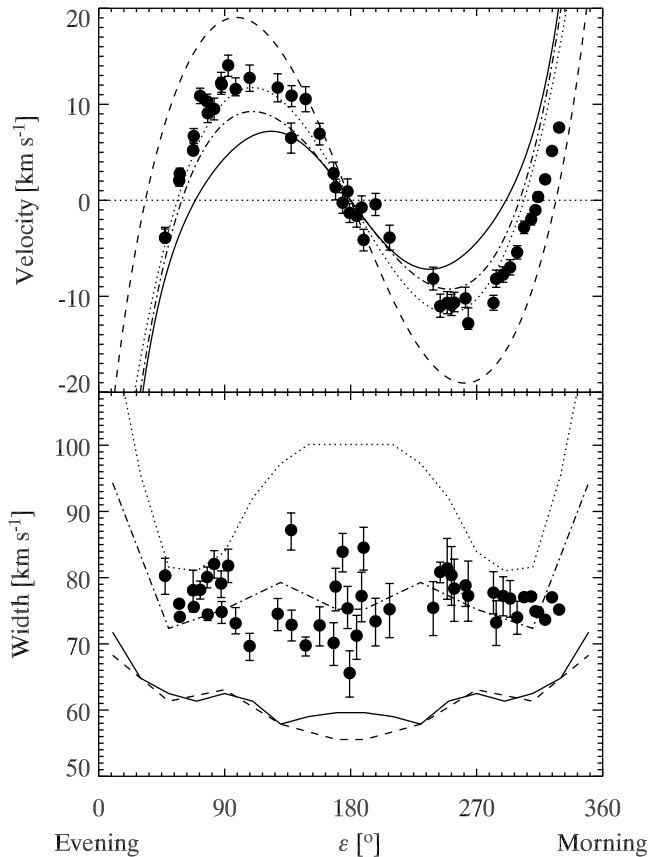


FIG. 5.—Predictions for the velocities and widths of the Mg I line from models of the zodiacal dust by Hirschi & Beard (1987) and Hirschi (1985): model *a* (solid line), particles on circular orbits and influenced only by solar gravity; model *b* (dotted line), particles on elliptical orbits with a uniform distribution of eccentricities between 0 and 1, randomly distributed perihelions, and no radiation pressure; model *c* (dot-dashed line), similar to model *b* above, but weighted toward lower eccentricities such that $n(e) \sim 1/e$; model *d* (dashed line), particles on circular orbits with a size distribution proportional to s^{-4} down to $\sim 0.5 \mu\text{m}$ and density 1 g cm^{-3} , resulting in a significant influence by solar radiation pressure that reduces the effective gravity. In all models the particle motion is parallel to the ecliptic plane, and in models *a*, *b*, and *c*, the particle number density decreases with distance from the Sun as $n(r) \sim r^{-1.5}$, taken from Table 2 in Hirschi & Beard (1987). For model *d*, $n(r) \sim r^{-2}$, and the velocities are taken from Table 4 in Hirschi (1985). A seventh-order polynomial passing through all the model data points was used to interpolate between model values for velocities.

experiencing radiation pressure. Figures 4*b* and 5 and Table 1 show that the profiles are broadened significantly with respect to the unperturbed solar profile and with respect to profiles predicted by models in which the dust is only in circular orbits. For example, Figure 6 compares the average spectrum for the five observations within 8° of $\epsilon = 180^\circ$ with the unperturbed solar spectrum. If all the orbits were circular and centered on the Sun, the profiles would be nearly identical. The broadening of the zodiacal profiles can only be explained by particles having radial components to their orbital motion.

4.2. Radiation Pressure and Orbital Inclinations

Orbital eccentricity alone is not sufficient to account for these observations. Although the predicted radial velocity variation from a dust population with a uniform distribution of orbital eccentricities (model *b*; dotted line) matches the observed radial velocities very well (Fig. 5*a*), the line widths predicted by this model are too large, especially near 180° (see Fig. 5*b*). The model that is weighted toward lower eccen-

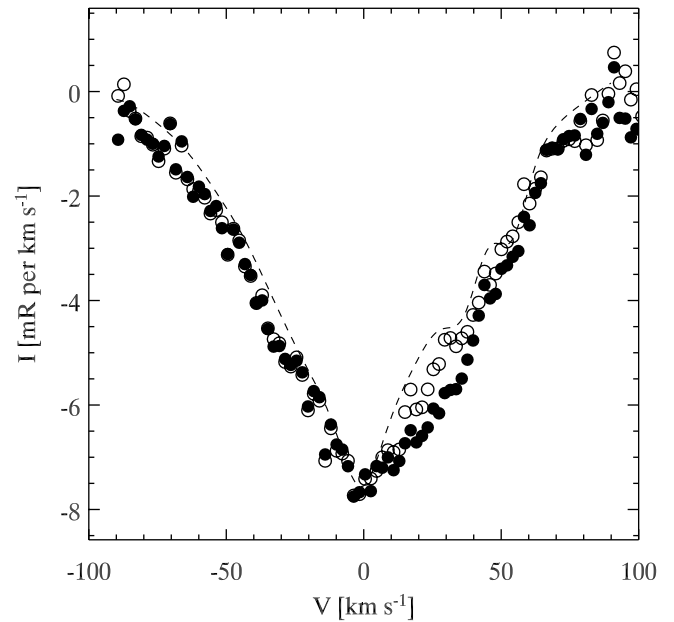


FIG. 6.—Mean spectrum for $\epsilon \approx 174^\circ\text{--}188^\circ$, showing that the antisolar zodiacal profile is broadened relative to the unperturbed solar profile (convolved direct solar spectrum; dashed curve). The filled and open symbols represent the profile with maximal and minimal corrections for the atmospheric contamination, respectively (see § 3.1 and Fig. 2*c*). The continua and minima of the profiles were made to coincide.

tricities (model *c*; dot-dashed line) provides a much better fit to the observed widths overall; however, that model does not predict a velocity amplitude as large as is observed. Models that combine eccentric orbits (to account for the line width) with an influence from radiation pressure (to increase the velocity amplitude) appear to be needed to obtain the best fit to the observed velocity variations and the line widths simultaneously (see Table 3, col [2] in Hirschi & Beard 1987). Another orbital parameter, which these models did not include, is inclination. Particles with a distribution of orbital inclinations will have smaller projected velocities along sight lines in the ecliptic plane. This will also increase the radial velocity amplitude (Rodriguez & Magro 1978) and thus mimic the effect of radiation pressure in observations confined to the ecliptic equator. Perhaps a combination of eccentricities and inclinations may even obviate the need for a significant effect from radiation pressure. The observations at high ecliptic latitude are therefore important for both probing the inclinations of the orbits and quantifying the influence of radiation pressure. Unfortunately, there are not yet models incorporating both eccentricity and inclination that predict both W and V .

A wide distribution of orbital inclinations is implied by the broad line profiles toward $\epsilon \approx 272^\circ$, $\beta \approx 47^\circ$ and the NEP (Table 1). The profile toward the NEP not only has one of the largest widths but, unlike profiles in all the other directions, has a distinctly flat-bottomed shape. The NEP spectrum and the unperturbed solar spectrum are shown in Figure 7. This substantial broadening of the profile toward the ecliptic pole, greater than that toward the antisolar direction, implies a population of particles that have significant components of their orbital velocities projected perpendicular to the ecliptic plane. For an orbital speed of 30 km s^{-1} near 1 AU, and neglecting the radial motion associated with eccentricity, the approximately $\pm 15\text{--}20 \text{ km s}^{-1}$ broadening at the base of the NEP profile suggests a distribution of inclinations extending up to

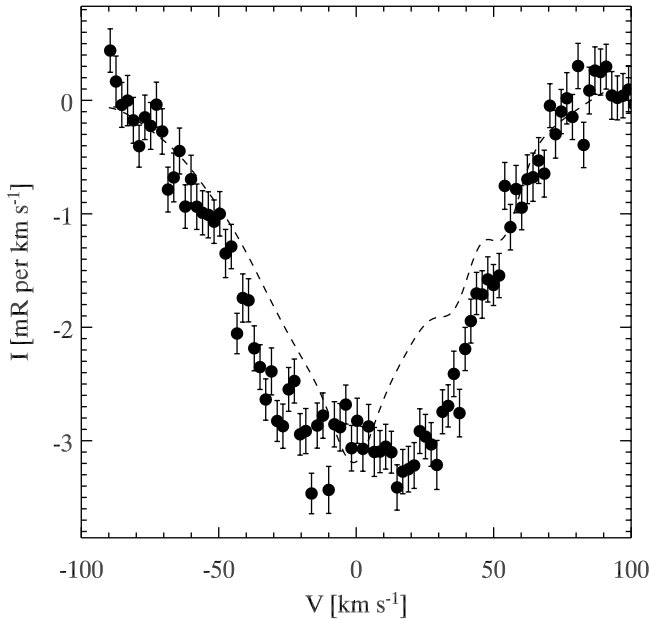


FIG. 7.—Zodiacal spectrum toward the NEP. The unperturbed solar profile is included for comparison. The error bars represent the $\pm 1 \sigma$ Poisson noise.

$\sim 30^\circ$ – 40° with respect to the ecliptic plane. This is close to but somewhat broader than the distribution derived from the *Galileo* and *Ulysses* in situ interplanetary dust impact detectors (Grün et al. 1997).

4.3. Line Profile Asymmetries

After removal of the atmospheric emission and taking into account the weak solar Fe and Cr features on the red side of the Mg I line (Fig. 1), we see no pronounced asymmetries in the shape of the zodiacal profiles. This places additional constraints on the properties of the zodiacal dust. For example, the nature of the scattering phase function of the dust is uncertain (e.g., Hahn et al. 2002), and Clarke et al. (1996) have shown that significant profile asymmetries will be present if the scattering function derived by Hong (1985) is used instead of isotropic scattering. In particular, they predicted that profiles between $\epsilon \approx 50^\circ$ and 70° and in the corresponding interval at $\epsilon \approx 290^\circ$ – 310° would have clearly extended wings on the red and blue sides, respectively. Another source of profile asymmetry would be a population of dust in retrograde motion. James (1969) calculated the radial velocities that would be associated with particles on retrograde orbits and showed that they would produce a Doppler-shifted absorption feature centered near $+55$ and -55 km s $^{-1}$ at $\epsilon \approx 50^\circ$ – 70° and $\epsilon \approx 290^\circ$ – 310° , respectively.

To search for these asymmetries, the mean spectrum within each of these two elongation intervals is plotted in Figure 8. To make the comparison easier, the mean spectrum toward $\epsilon \approx 50^\circ$ – 70° was shifted 9.0 km s $^{-1}$ to the blue so that the minima of the two profiles coincide. Within the scatter of the data points, the profile shapes appear to be nearly identical, indicating that there are no pronounced asymmetries produced by retrograde particles or the scattering discussed above. For example, the absence of a significant depression on the red side of the evening spectrum (*open circles*) relative to that part of the morning spectrum (*filled circles*), and vice versa for the blue side, indicate that any population of retrograde particles must be less than 10% the prograde population.

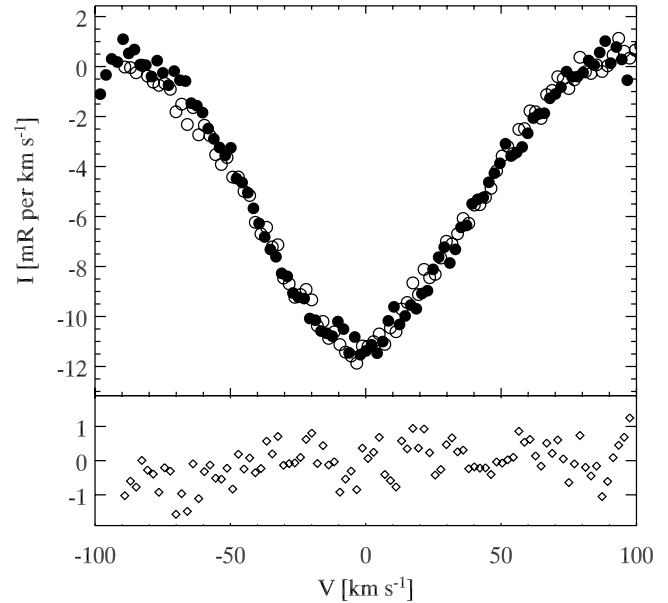


FIG. 8.—Average spectrum between $\epsilon \approx 50^\circ$ and 70° (*open symbols*) and the average spectrum between $\epsilon \approx 290^\circ$ and 310° (*filled symbols*) have been superposed to search for asymmetries in the line profiles (see § 4.3). To make the comparison easier, the former spectrum was shifted -9.0 km s $^{-1}$ with respect to the latter spectrum. The difference between the two profiles is also plotted (*open diamonds*).

The spectra toward 180° and the NEP show marginal evidence for extra absorption on the red side of the profiles near $+30$ km s $^{-1}$ (Figs. 6 and 7). This could be an indication of a small population of particles with a radial outflow (Hirschi 1985); however, given current uncertainties associated with the removal of terrestrial emission (e.g., Fig. 6), it is difficult to judge its significance. A more extensive observational program, including studies of more than one Fraunhofer line, are needed to characterize more accurately such subtle asymmetries (see below).

5. CONCLUSIONS AND FUTURE OBSERVATIONS

Observations of the Mg I $\lambda 5184$ line with WHAM have demonstrated that high-throughput spectroscopic measurements of scattered solar Fraunhofer line profiles in the zodiacal light can be a useful tool for exploring the properties of the zodiacal dust, as suggested by Ingham (1963), James (1969), and others. These observations, combined with models of the zodiacal cloud, have probed or placed constraints on the retrograde and prograde populations, the orbital eccentricities and inclinations, the effects of nongravitational forces, and the scattering properties of the particles. Furthermore, this characterization of the Doppler distortions of Fraunhofer profiles in the zodiacal light should facilitate a more accurate removal of zodiacal contamination in other astrophysical observations (see, e.g., Haffner et al. 2003). The detection of the extremely weak telluric emission lines also implies that caution must be used in the interpretation of line profiles, equivalent widths, line intensities, and the nature of the continuum in low-resolution ground-based spectra of zodiacal light and other low surface brightness astrophysical sources.

These results also point to ways in which observations can be further improved. For example, integration times can be significantly lengthened to increase the signal-to-noise ratio, and the bandwidth of the spectra could be expanded to make it possible to define the continuum more accurately. A fuller

sampling at higher ecliptic latitudes would also help to characterize more accurately particle orbits inclined to the ecliptic plane (Rodriguez & Magro 1978). Systematic errors associated with the removal of the atmospheric emission lines, the largest source of uncertainty in the measurements of radial velocities and profile shapes, could be reduced by observing two Fraunhofer lines (e.g., Mg I λ 5173 in addition to Mg I λ 5184). Both lines are modified identically by scattering from the zodiacal dust but are affected differently by the atmospheric foreground emission. A complete set of such spectra obtained multiple times over the course of a year or more would also allow a search for more subtle effects associated with possible azimuthal asymmetries in the zodiacal cloud, the inclination of the Earth's orbit with respect to the dust plane, and the eccentricity of the Earth's orbit (e.g., Dermott et al. 1994; Kelsall et al. 1998). In addition, because observations toward the same elongation at different times of the year sample different parts of the Milky Way, observations spread throughout the year could help to characterize and remove

any spectral features associated with the background starlight (Mattila 1980). A more accurate unperturbed source spectrum (free of any Ring effect) could be obtained from observations of the Moon, rather than the twilight sky. The WHAM facility provides an opportunity to carry out such an investigation. The proper interpretation of these data also requires a more complex grid of models, incorporating a range of orbital and scattering parameters and particle distributions (e.g., Haug 1958) that predict the velocities and shapes of the zodiacal line profiles over the sky.

We thank Matt Haffner, Kurt Jaehnig, and Steve Tufte for their valuable contributions to the operation of WHAM, Alexander Kutyrev for his assistance and encouragement, and the anonymous referee for helpful comments. We are also grateful to Dean Hirschi for providing a copy of his Ph.D. thesis. The WHAM program is supported by the National Science Foundation through grant AST 02-04973.

REFERENCES

- Bandermann, L. W., & Wolstencroft, R. D. 1969, *Nature*, 221, 251
 Bernstein, R. A., Freedman, W. L., & Madore, B. F. 2002, *ApJ*, 571, 85
 Clarke, D., Daehler, M., Mack, J. E., Ring, J., & Stoner, J. O. 1967, in *Modern Astrophysics: A Memorial to Otto Struve*, ed. M. Hack (Paris: Gordon & Breach), 43
 Clarke, D., Matthews, S. A., Mundell, C. G., & Weir, A. S. 1996, *A&A*, 308, 273
 Daehler, M., Mack, J. E., Stoner, J. O., Clarke, D., & Ring, J. 1968, *Planet. Space Sci.*, 16, 795
 Delbouille, L., Neven, L., & Roland, C. 1973, *Photometric Atlas of the Solar Spectrum from λ 3000 to λ 10000* (Liège: Inst. Astrophys., Univ. Liège)
 Dermott, S. F., Jayaraman, S., Xu, Y. L., Gustafson, B. Å. S., & Liou, J. C. 1994, *Nature*, 369, 719
 East, I. R., & Reay, N. K. 1984, *A&A*, 139, 512
 Fried, J. W. 1978, *A&A*, 68, 259
 Grainger, J. F., & Ring, J. 1962, *Nature*, 193, 762
 Grün, E., et al. 1997, *Icarus*, 129, 270
 Haffner, L. M., Reynolds, R. J., Tufte, S. L., Madsen, G. J., Jaehnig, K., & Percival, J. 2003, *ApJS*, 149, 405
 Hahn, J. M., Zook, H. A., Cooper, B., & Sunkara, B. 2002, *Icarus*, 158, 360
 Haug, U. 1958, *Z. Astrophys.*, 44, 71
 Hausen, N. R., Reynolds, R. J., Haffner, L. M., & Tufte, S. L. 2002, *ApJ*, 565, 1060
 Hicks, T. R., May, B. H., & Reay, N. K. 1974, *MNRAS*, 166, 439
 Hirschi, D. C. 1985, Ph.D. thesis, Univ. Kansas
 Hirschi, D. C., & Beard, D. B. 1987, *Planet. Space Sci.*, 35, 1021
 Hong, S. S. 1985, *A&A*, 146, 67
 Huestis, D. L., Ali, S., Cosby, P. C., & Slinger, T. G. 2001, *BAAS*, 33, 1111
 Ingham, M. F. 1963, *MNRAS*, 126, 377
 James, J. F. 1969, *MNRAS*, 142, 45
 ———. 1996, *MNRAS*, 280, 1055
 James, J. F., & Smeeth, M. J. 1970, *Nature*, 227, 589
 Kattawar, G. W., Young, A. T., & Humphreys, T. J. 1981, *ApJ*, 243, 1049
 Kelsall, T., et al. 1998, *ApJ*, 508, 44
 Mann, I. 1998, *EP&S*, 50, 465
 Mann, I., Grün, E., & Wilck, M. 1996, *Icarus*, 120, 399
 Mattila, K. 1980, *A&A*, 82, 373
 Morgenthaler, J. P., et al. 2001, *ApJ*, 563, 451
 Mukai, T., & Mann, I. 1993, *A&A*, 271, 530
 Nossal, S., Roesler, F. L., Bishop, J., Reynolds, R. J., Haffner, L. M., Tufte, S. L., Percival, J., & Mierkiewicz, E. Z. 2001, *J. Geophys. Res.*, 106, 560
 Pallamraju, D., Baumgardner, J., & Chakrabarti, S. 2000, *Geophys. Res. Lett.*, 27, 1875
 Reay, N. K. 1969, *Nature*, 224, 54
 Reay, N. K., & Ring, J. 1969, *Planet. Space Sci.*, 17, 561
 Reynolds, R. J., Roesler, F. L., & Scherb, F. 1973, *ApJ*, 179, 651
 Rodriguez, G. L., & Magro, C. S. 1978, *A&A*, 64, 161
 Sioris, C. E., & Evans, W. F. J. 1999, *Appl. Opt.*, 38, 2706
 Tufte, S. L. 1997, Ph.D. thesis, Univ. Wisconsin, Madison